



Development of RF windows for 650 MHz multibeam klystron

Sheng-Chang Wang¹ · Zu-Sheng Zhou² · Zhi-Jun Lu² · Zhi-Qing Liu³ · Shigeki Fukuda⁴ · Yu Liu² · Jing-Yi Li² · Wei-Ming Li¹

Received: 22 February 2023 / Revised: 16 June 2023 / Accepted: 20 June 2023 / Published online: 21 September 2023

© The Author(s), under exclusive licence to China Science Publishing & Media Ltd. (Science Press), Shanghai Institute of Applied Physics, the Chinese Academy of Sciences, Chinese Nuclear Society 2023

Abstract

Radio frequency windows are developed and evaluated for a 650 MHz continuous-wave multibeam klystron. Thin-pillbox windows with alumina and beryllia disks are designed with an average RF power of CW 400 kW. Results of a cold test and tuning procedures are described. The final measured S11 curves under the required bandwidth are less than -32.0 and -26.9 dB for alumina and beryllia windows, respectively. The windows are tested up to CW 143 kW for traveling waves and CW 110 kW for standing waves using a solid-state amplifier as an RF power source. Multipactor simulations for windows and benchmark studies for the thermal analysis of ceramic disks are introduced.

Keywords RF window · High-power test · MBK

1 Introduction

The circular electron positron collider (CEPC) [1] is a significant international scientific project. To reduce the high cost of power consumption, klystrons operating at 650 MHz with a high efficiency are required. The multibeam klystron (MBK), which can offer high efficiencies and low gun voltages, is designed as a candidate for CEPC radio frequency (RF) power sources [2, 3]. In the CEPC MBK configuration, two thin-pillbox windows are connected to the output cavity in opposite directions. As a crucial component of the CEPC MBK, the individual output window operates at a continuous wave (CW) of 400 kW while maintaining the integrity of the vacuum envelope for the MBK. A schematic

illustration of the CEPC MBK and its output windows are shown in Fig. 1. Table 1 lists the design parameters of the CEPC MBK.

As listed in Table 2, pillbox windows are typically adopted in L-band pulsed MBKs [4]. The pillbox windows in Table 2 exhibit a mutual characteristic of $D \sim \sqrt{a^2 + b^2}$, where D is the diameter of the ceramic disk, a the longest dimension of the waveguide, and b the shortest dimension of the waveguide. A coaxial window is typically adopted for an L-band CW klystron, which is typically a single-beam klystron (SBK) [4]. The CEPC MBK, which operates in CW mode, is designed with a thin-pillbox window instead of a coaxial window to achieve a simpler output structure, additionally, the diameter of the ceramic disk is specified to be less than the shortest dimension of the waveguide ($D \leq b$). It is be risky if the CEPC MBK adopts the common pillbox window, for example, the average output power of the MBKs in Table 2 is lower than 150 kW, let alone the large size and high weight of the output windows derived from the WR1500 waveguide.

The pillbox window with $D \leq b$, which was designed for the RF transfer system of particle accelerators, has been tested up to CW 500 kW [5] and CW 800 kW [6]. However, the usage on UHF-band klystrons is rarely reported. In this study, thin-pillbox window prototypes featuring $D \leq b$ with alumina and beryllia disks are designed, manufactured, and evaluated. A tuning procedure and cold tests for self-matching windows are introduced. In addition, a

✉ Sheng-Chang Wang
wangshengchang@hotmail.com

✉ Zu-Sheng Zhou
zhouzs@ihep.ac.cn

¹ National Synchrotron Radiation Laboratory, University of Science and Technology of China, Hefei 230026, China

² Institute of High Energy Physics, Chinese Academy of Sciences, Beijing 100049, China

³ Kunshan Guo Li Electronic Technology Co., Ltd., Kunshan 215300, China

⁴ High Energy Accelerator Research Organization, KEK 1-1 Oho, Tsukuba, Ibaraki 305-0801, Japan

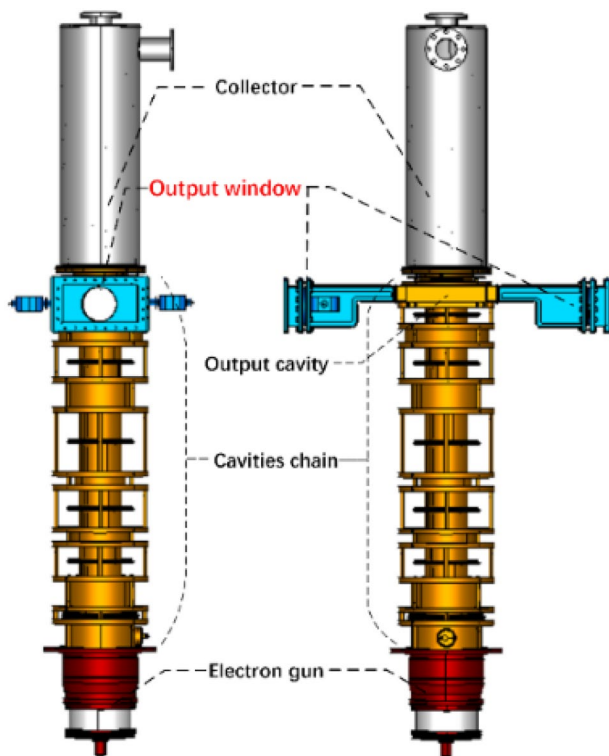


Fig. 1 (Color online) Schematic illustration of CEPC MBK and its output windows

Table 1 Designed parameters of CEPC MBK

Parameters	Value
Frequency (MHz)	650
Voltage (kV)	54
Current (A)	20.8
Beam No	8
Output power (kW)	800
-1 dB bandwidth (MHz)	± 0.5
Output window/Waveguide standards	Thin-pillbox window/ WR1500

multipactor simulation and a benchmark for thermal analysis are presented.

Section 2 describes the RF design and tolerance analysis [7] for the windows. The assembly diagram, cold-test results, and tuning procedure for the window prototypes are introduced in Sect. 2. The details of the high-power test of the prototype windows and thermal analysis are described in Sect. 3. A multipactor simulation is presented in Sect. 4. Finally, the conclusions are presented in Sect. 5.

2 Window design and cold test

2.1 Considerations regarding dielectric material

Because water cooling occurs on the perimeter of the ceramic disk and the thermal conductivity of the dielectric material (e.g., alumina) is low, a temperature difference can be generated between the center and perimeter. Consequently, the thermal stress can exceed the mechanical strength and result in the fracture of the ceramic disk. Hence, the dielectric loss tangent of the ceramic should be low, whereas the thermal conductivity should be high. However, identifying a dielectric material that possesses both required properties is difficult. In this study, alumina with a low dielectric loss tangent and beryllia [8] were used. Two types of windows were designed and evaluated for comparison. Detailed properties and information regarding the selected materials are listed in Table 3. As the dielectric loss tangent presented in Table 3 is not precise, it is inadequate for achieving an accurate thermal simulation. In addition, the actual loss factor should include the contribution of the antimultipactor layer.

2.2 RF design and tolerance analysis

As mentioned in [11], an S11 of -30 dB from the cold test is considered acceptable for high-power testing. Because the dielectric constant error and mechanical error would deteriorate S11 in a cold test, the design value for S11 should be less than -60 dB to achieve a sufficient margin.

The dielectric constants of the beryllia listed in Table 3 are imprecise. Small samples were sent to a third-party testing center, and the obtained dielectric constant was 7.1 (@1 MHz). The dimensions of the waveguide window are shown in Fig. 2, which shows the shortest side of the waveguide. The structures of the alumina and beryllia windows were similar, and their dimensions were slightly different. A thin pillbox was connected to the WR1500 waveguide on both its sides. On the vacuum side, the waveguide was reduced to one-third of its shortest dimensions to match the output cavity of the MBK as well as to avoid interference with the other sections of the MBK, e.g., the focusing magnet.

Using the Frequency Domain Solver of the CST STUDIO SUITE [12], the S11 of the alumina and beryllia windows were optimized [13, 14], as shown in Fig. 3a, b, respectively. The required mechanical errors of A (thickness of the ceramic disk), B (diameter of the ceramic disk), and C (length of the thin pillbox) were ± 0.02 , ± 0.1 , and ± 0.1 mm, respectively. The tolerance analysis indicates that the effects of the window dimensions (A, B,

Table 2 L-band klystrons and their output windows

Klystron type	Frequency (MHz)	Peak output power (MW)	Average output power (MW)	Output window type	<i>a</i> (mm)	<i>b</i> (mm)	Number of output window
E37503 MBK	999.516	20	0.15	Pillbox window	247.65	146.05	1
E3736 MBK	1300	10	0.15	Pillbox window	165.10	82.55	2
TH1803 MBK	999.516	20	0.15	Pillbox window	247.65	146.05	2
TH1801 MBK	1300	10	0.15	Pillbox window	165.10	82.55	2
VLK8601 MBK	1300	10	0.15	Pillbox window	165.10	82.55	2
VKP7952A SBK	700	1	1	Coaxial window	–	–	1
CEPC MBK	650	0.8	0.8	Thin-pillbox window	381.00	190.50	2

Table 3 Material properties

Items	Alumina (AO479U) [9]	Beryllia (B-99) [10]
Dielectric constant	10 @ 1 MHz	6.5~7.3 @ 1 MHz
Dielectric loss tangent	$< 1 \times 10^{-4}$ @ 1 MHz	$\leq 4 \times 10^{-4}$ @ 1 MHz
Thermal conductivity	32 W/(m K)	240 W/(m K)
Dielectric strength	17.5 MV/m	20 MV/m
Purity	99.6%	99%
Tensile Strength	260 MPa	140 MPa

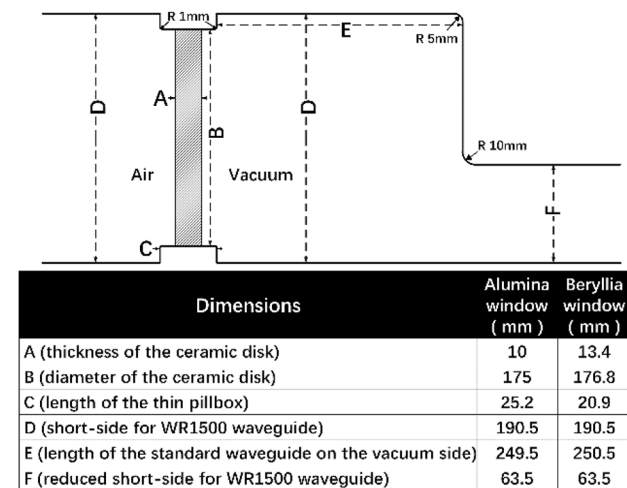


Fig. 2 Dimensions of thin-pillbox windows

and C) on S11 is negligible if mechanical errors are guaranteed. Additionally, the dielectric constants should be emphasized because the values in Table 3 and from the third-party testing center are specified as 1 MHz without any error range. We applied a tuning procedure based on the assumption that the measured S11 diverges from the simulated prediction for the first time because of errors

arising from the dielectric constants used in the simulation (see Sect. 3).

2.3 Cold test and tuning procedure

The outline and assembly diagrams of the window are shown in Fig. 4a, b, respectively. The window was primarily composed of oxygen-free copper (OFC) waveguides, a thin pillbox, and a dielectric ceramic disk. Ceramic disks and thin pillboxes were brazed with Ag–Cu-based fillers. The thin pillbox and window iris were welded using an electron beam. Meanwhile, the waveguides were brazed from the OFC plates and welded to the iris and thin-pillbox assembly.

On the vacuum side, stainless-steel plates were brazed on the outer surface of the OFC waveguides to prevent waveguide deformation due to atmospheric pressure. Sight glass [15] and vacuum sealing flanges were used only on the window prototypes to facilitate the high-power RF experiment. A rectangular OFC ring was placed between the rectangular waveguide and the window iris on the vacuum side for frequency tuning. Owing to the different thicknesses of the OFC ring, dimension E in Fig. 2 can be adjusted, and the center frequency of S11 can be adjusted during the cold test. The window was pre-assembled for S11 measurement, and the final welding was performed after the thickness of the OFC ring was selected based on the simulation and cold test results.

As mentioned in the previous section, based on tolerance analysis, we applied a tuning procedure based on the assumption that the main error originated from the uncertainty of the dielectric constant.

- i. The window was assembled and S11 was measured for the first time. The measured center frequencies of the S11 were 649.5 and 651.3 MHz for the alumina and beryllia windows, respectively.
- ii. The simulation was repeated using the modified dielectric constant until the simulated center frequency agreed with the S11 measured from the previous step.

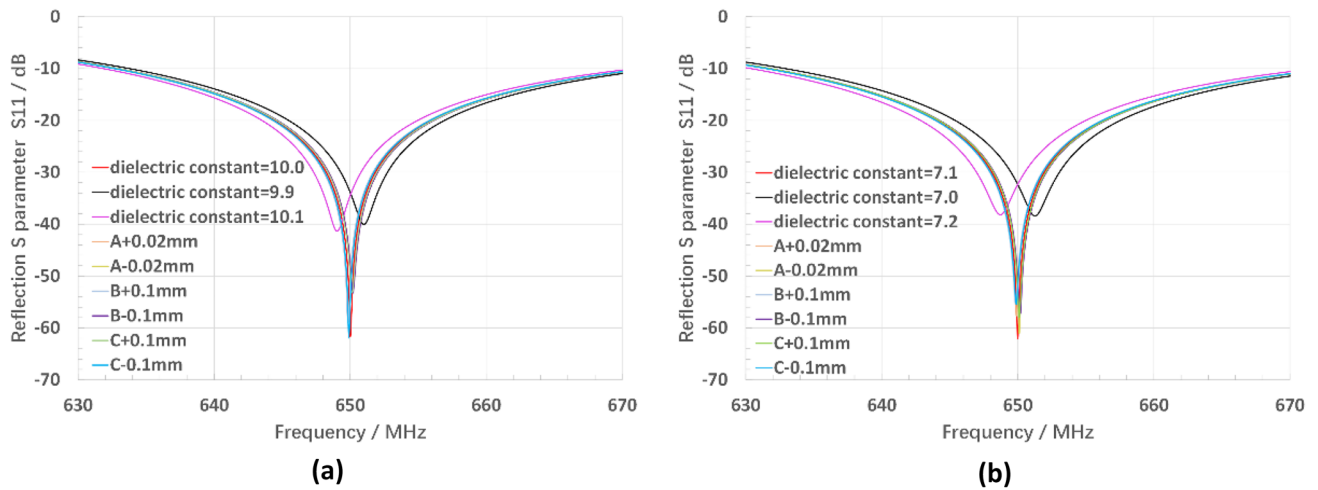
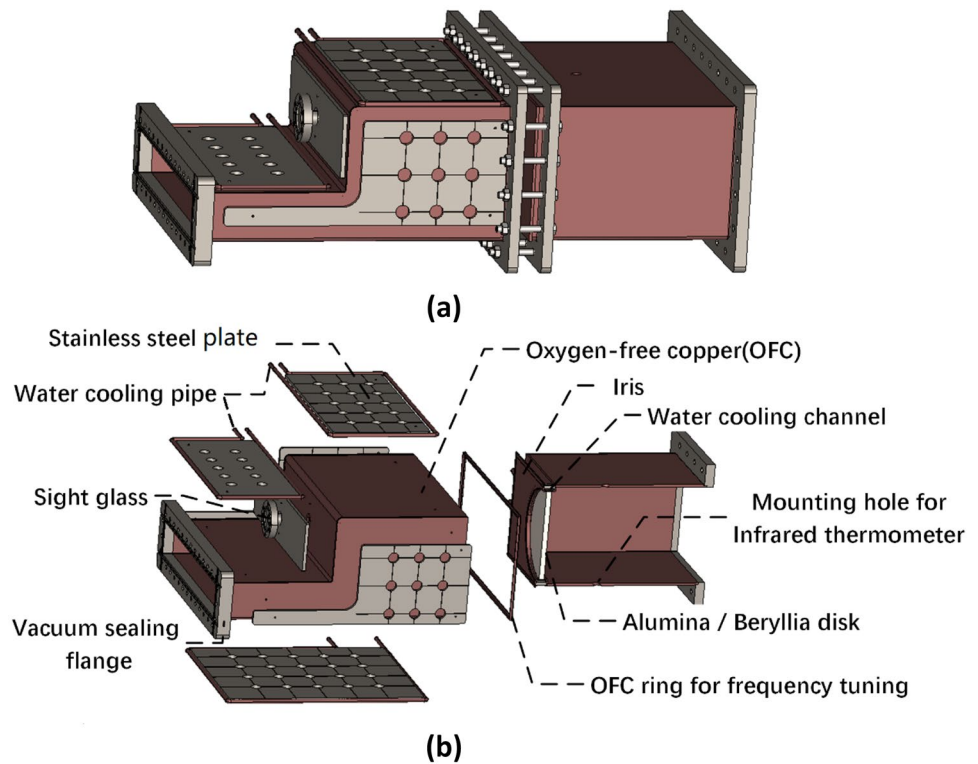


Fig. 3 Simulated S11 including effects of dielectric constant and window dimensions on reflection characteristics: **a** alumina window; **b** beryllia window

Fig. 4 (Color online) **a** Outline of alumina/beryllia window; **b** assembly diagram of alumina/beryllia window



Subsequently, dimension E was adjusted such that the simulated center frequency returned to 650.0 MHz. In our case, the dielectric constants were modified from 10 to 10.05 and from 7.1 to 6.9, and the dimension E was modified from 249.5 to 249.0 mm and 250.5 to 252.5 mm for the alumina and beryllia windows, respectively.

- iii. The thickness of the rectangular OFC ring was adjusted based on the dimension E adjusted in the

simulation in the previous step. Subsequently, the window was reassembled for the second measurement of S11. In our case, the second measured S11 agreed well with the simulated S11 after the dielectric constant and dimension E were corrected, as shown in Fig. 5a, b. For the alumina window, the measured S11 were -32.1, -35.0, and -32.0 dB at frequencies of 651, 650, and 649 MHz, respectively. For the beryllia window, the measured S11 values were -27.0, -27.5, and

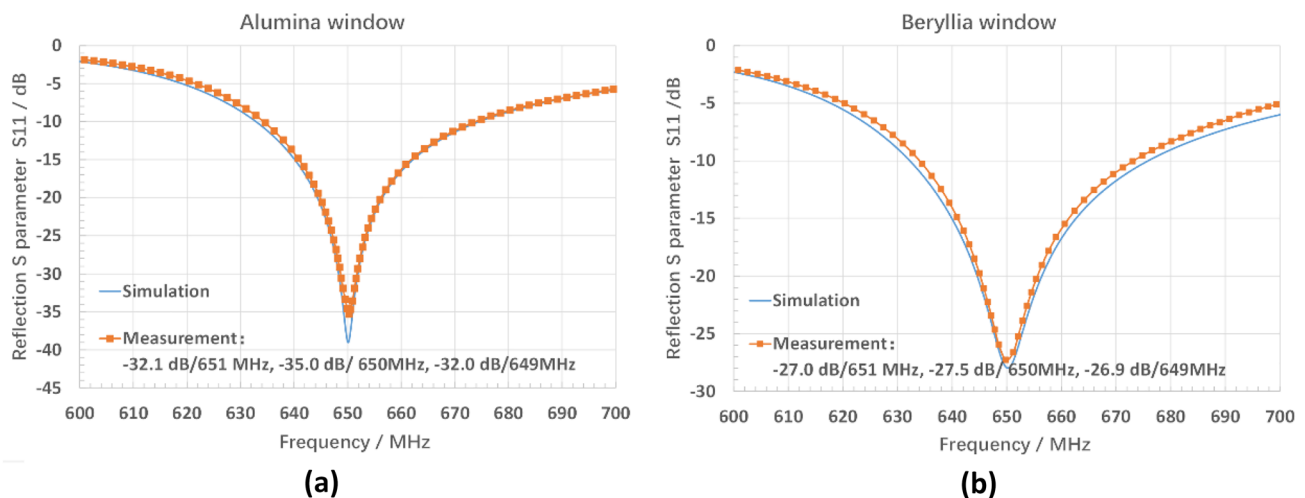


Fig. 5 (Color online) Simulated S11 after correction of dielectric constant and dimension E, and measured S11 after adjustment of OFC ring thickness for **a** alumina window and **b** beryllia window

−26.9 dB at frequencies of 651, 650, and 649 MHz, respectively.

For the beryllia window, the measured S11 did not reach the goal of −30 dB because of an error in the dielectric constant. As the VSWR values were less than 1.1 in the operating bandwidth for both the alumina and beryllia windows, we accepted the cold test results.

3 Thermal analysis and high-power test

Because thermal failure is the main cause of window breakdown under a high average power [16], a thermal analysis was performed. The cooling channels on the perimeter of the ceramic disk and the cooling pipes on the OFC waveguide are shown in Fig. 4b. The heat factor should include the dielectric loss tangent of the ceramic disk and the Ohmic loss factor of the antimultipactor layer. The thermal conductivity values for the thermal analysis are listed in Table 3. A plot of the maximum temperature increase on the ceramic disk vs. the heat factor under a traveling wave (TW) power of 400 kW is shown in Fig. 6a, along with a plot of the maximum thermal stress vs. the heat factor. As an example, the distributions of the temperature increase and thermal stress on the beryllia disk with a TW power of 400 kW and a heat factor of 4×10^{-4} are shown in Fig. 6b. Some studies [17] recommended thermal stresses not exceeding 25% of the ceramic's tensile strength as a conservative limit. Accordingly, the conservative limits for the heat factor should be 9.0×10^{-5} and $4.5E-4$ for the alumina and beryllia disk, respectively. Accurate heat factors can be obtained from the benchmark of the thermal simulation by measuring the

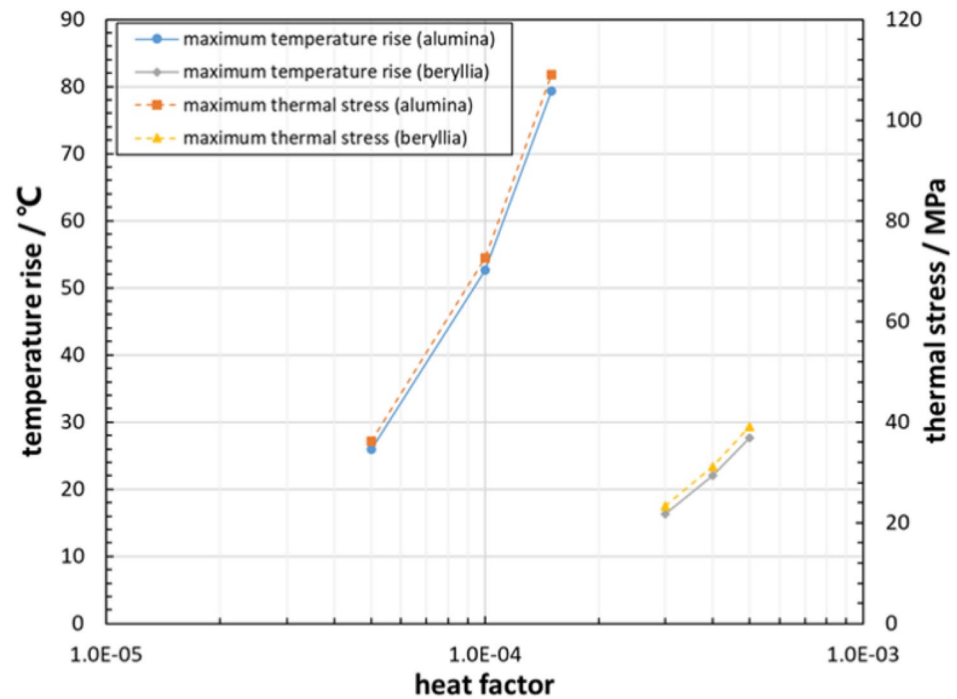
temperature increase on the ceramic disk during the high-power test.

One alumina window and one beryllia window were manufactured as prototypes for the high-power tests. Figure 7a shows a photograph of the alumina and beryllia windows connected back-to-back in a stainless-steel vacuum chamber. Vacuum-sealing flanges for connecting the stainless-steel vacuum chambers were not used in the CEPC MBK. The window waveguide was welded to the output waveguide of the CEPC MBK. Sight glasses were designed on the window prototypes to monitor the glow of the multipactor during the test. Similarly, it was not adopted in the CEPC MBK window. Cooling pipes were welded to the copper waveguides of the window. The stainless-steel vacuum chamber featured water cooling on the longest side surface. However, the shortest-side surface had no cooling, which limited its power level during high-power testing.

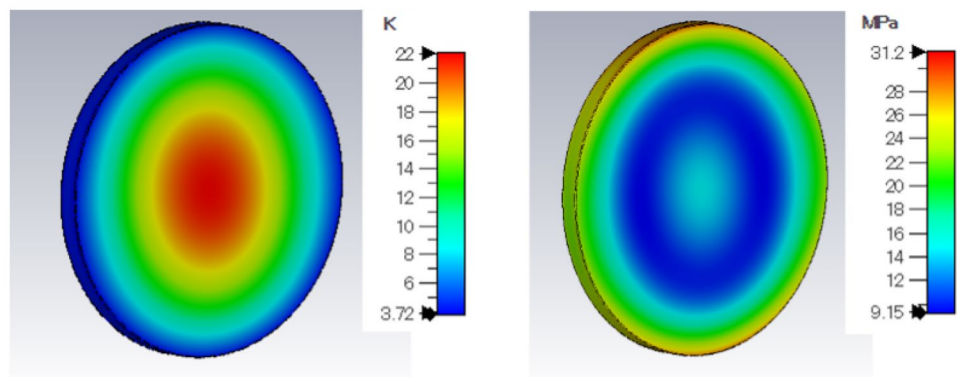
Because an RF power source to accomplish a TW high-power test exceeding 400 kW is not available, we employed a solid-state amplifier (SSA) with a rated power of 150 kW to perform a standing wave (SW) test [18, 19]. Because the dielectric losses under a SW can be four times those under a TW, the 150 kW SSA is qualified for evaluating the windows in terms of dielectric losses and temperature increase.

The TW test was performed prior to the SW test. As shown in Fig. 7b, the output waveguide of the SSA was connected to the air side of the beryllia window. The beryllia window was connected to the alumina window through the vacuum chamber, as described above. The air side of the alumina window was associated with the RF water load. Two cameras were mounted on Sight glasses to monitor the surfaces of the ceramic disks (not shown in Fig. 7b). Two infrared thermometers were mounted in the holes of the air-side

Fig. 6 (Color online) **a** Plots of maximum temperature increase and thermal analysis on ceramic disk vs. heat factor; **b** distributions of temperature increase and thermal stress on beryllia disk with CW travelling wave RF power of 400 kW and heat factor of 4×10^{-4}



(a)



(b)

waveguides (not shown in Fig. 7b) to monitor the maximum temperature of the ceramic disk. A directional coupler and RF water load were used to measure the RF power.

After establishing the test setup, as shown in Fig. 7b, some copper-to-copper welding seams on the alumina window waveguide leaked. The leakage was rectified using a resin and epoxy. Subsequently, the vacuum leakage rate was 4×10^{-11} mbar L/s. The vacuum section was baked at 80°C – 90°C for 48 h. The ultimate vacuum pressure reached $4\text{E-}7$ Pa after the high-power tests were completed. Under the CW RF power, the vacuum pressure increased owing to the heating of the ceramic disks and stainless-steel vacuum chamber. During the high-power test, a fast vacuum interlock at $1\text{E-}5$ Pa was used to turn off the driving power of the SSA [20].

During initial processing, a short RF pulse with a duty as low as 0.1% was applied until a peak power of 150 kW was attained [21]. During this initial process, outgassing occurred once a new peak RF power was reached. Approximately 24 h were required to attain 150 kW. In the second process, approximately 12 h was required to expand the RF duty from 0.1% to 1% with rare outgassing. The RF duty expanded rapidly from 1 to 100% owing to the absence of outgassing or interlocking. The measured saturated output power of the SSA was 143 kW. The windows were tested under saturated output power for more than 4 h. As listed in Table 4, the temperature increase on the ceramic disks under CW 143 kW was measured to be 10.2 ± 1.0 and 8.7 ± 1.0 °C for alumina and beryllia, respectively. The infrared thermometer featured a measuring error of ± 1.0 °C.

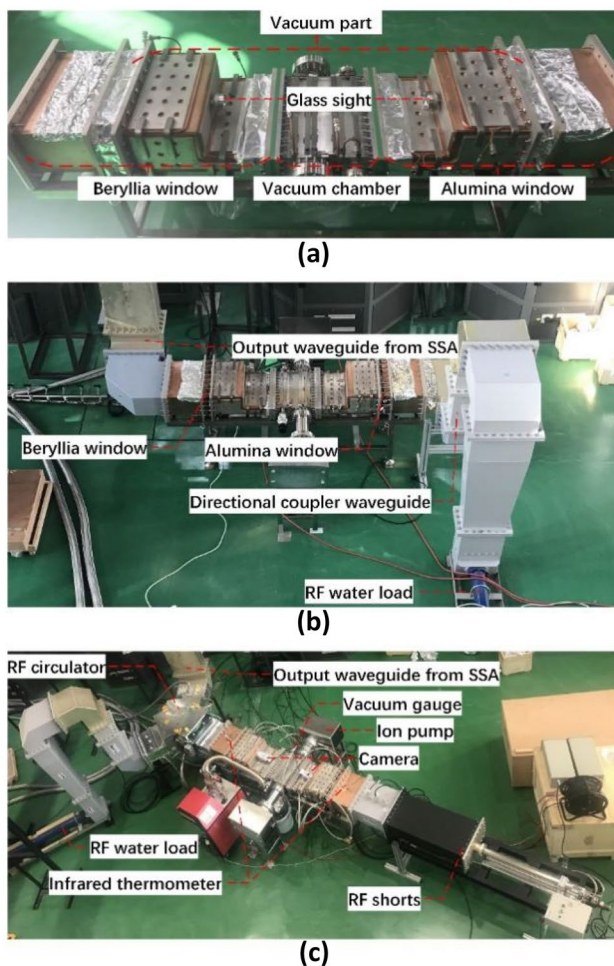


Fig. 7 (Color online) **a** Photograph of alumina and beryllia windows connected back-to-back through a stainless vacuum chamber; **b** photograph of test setup for traveling wave (TW) high-power test; **c** photograph of test setup for standing wave (SW) high-power test

No multipactor glow was captured by the cameras during the TW processing. Subsequently, the vacuum section was charged with nitrogen, and the windows were retested under CW 143 kW. The ceramic disks exhibited the same temperature increase under vacuum and nitrogen-filled conditions. This proves that multipacting did not occur in the alumina and beryllia windows in the TW test.

The test setup was reconstructed for the SW test, as shown in Fig. 7c. An RF circulator was connected between the output waveguide of the SSA and the air-side waveguide

of the beryllia window. An RF-short was connected to the air side of the alumina window. The reflected face was rendered mobile such that the antinode of the SW can be adjusted to the alumina and beryllia disks separately. First, the antinode of the SW was adjusted to the beryllia disk. An RF pulse with a duty of 5% was applied and 3 h was required to reach 150 kW under the same duty. During the expansion of the RF duty, the vacuum pressure increased gradually and reached the interlock level owing to the heating of the beryllia disk and stainless vacuum chamber. The temperature of the shortest-side face of the stainless-steel vacuum chamber increased owing to inadequate water cooling. The vacuum pressure decreased rapidly after interlocking. After 30 s, the RF power resumed, and the vacuum pressure increased gradually. After approximately 75 h of RF conditioning, the RF duty was expanded to a CW and the power was 115 kW, which remained as such for more than 3 h without an interlock. Accordingly, the temperature increase in the beryllia disk was measured to be 28.4 ± 1.0 °C. Second, the antinode of the SW was adjusted to the alumina disk. A total of 20 h was required to reach a CW RF power of 110 kW, which remained as such for more than 3 h without an interlock. The temperature increase exhibited by the alumina disk was measured to be 37.0 ± 1.0 °C.

A benchmark study pertaining to the temperature simulation of a ceramic disk under TW and SW conditions was conducted. Once the heat factor, including the dielectric loss tangent of the ceramic disk and the Ohmic loss factor of the antimultipactor layer, reached 6×10^{-5} and 4×10^{-4} for the alumina and beryllia disks, respectively, the simulated temperature increases of the alumina disk and beryllia disk were within or extremely similar to the error range of the measured temperature increases, as listed in Table 4. The benchmarked heat factors were below the conservative limits for both the alumina and beryllia disks. Therefore, the alumina and beryllia disks were both qualified from the perspective of thermal stress.

4 Multipactor simulation

The multipactor in a window is a combined effect of the RF field and secondary electron emission from a dielectric or metal. The multipactor near the ceramic surface, which may result in localized surface melting [22] or contribute to

Table 4 Measured and simulated temperature increases on alumina and beryllia disks

	TW CW 143 kW	SW CW 110 kW	SW CW 115 kW
Alumina disk (measurement)	10.2 ± 1 °C	37 ± 1 °C	–
Alumina disk (simulation)	11.6 °C	36.1 °C	–
Beryllia disk (measurement)	8.7 ± 1 °C	–	28.4 ± 1 °C
Beryllia disk (simulation)	8.4 °C	–	°C

the total thermal loss [23] of the ceramic disk, contributes significantly to window failure. The particle-in-cell (PIC) [24] computation of the CST STUDIO SUITE [12] was applied to evaluate the severity of the multipactor effect in a thin-pillbox window. The CST PIC Solver can monitor the emitted secondary particle number over time as well as the total particle number in the simulated space. The CST Help Document indicates that the criterion for a multipactor phenomenon is the detection of the exponential growth of the emitted secondary electrons [12].

All inner surfaces of the vacuum metal waveguide were set as electron emission sources. The DC emission model was selected for primary electrons [25] with a random emission energy of 0–6 eV and a random emission angle [26]. The RF fields were imported from the CST Frequency Domain Solver. The secondary-electron-yield (SEY) curves of alumina [27], beryllia [27], copper as-received [28], and copper after baking [28] imported for the simulation are shown in Fig. 8.

In the first step, only the SEYs of the ceramic disks were included in the simulation [29]. As shown in Fig. 9a, the total number of electrons in the vacuum space of the alumina

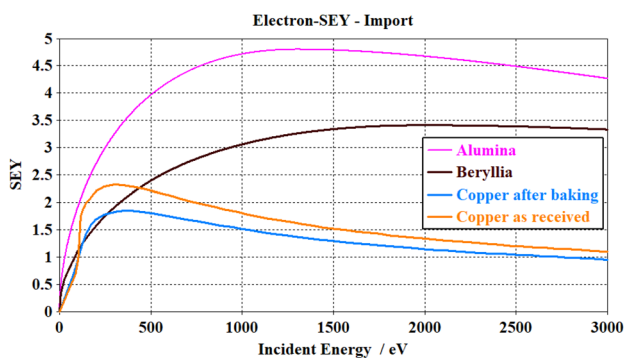


Fig. 8 (Color online) Secondary-electron-yield (SEY) curves imported for simulation

window indicated no growth after 50 ns under TW powers of 100, 200, and 400 kW. As shown in Fig. 9b, even when the total electron number was in the 1×10^6 range, the secondary electron numbers were negligible owing to the small electric-field component perpendicular to the ceramic surface. The beryllia window exhibited similar simulation results under the same conditions.

The SEY of copper was included in the simulation as well. As shown in Fig. 10a, once the copper state reached the as-received state and the TW power was as high as 400 kW, the secondary electrons emitted in the alumina window grew exponentially, which fulfills the criterion of the multipactor. After baking, the growth of the emitted secondary electrons decelerated. Under TW powers of 100 and 200 kW, the growth of the emitted secondary electrons with copper after baking was slower than that with the as-received copper as well. In our study, the copper plates were brazed in a vacuum furnace to bake the copper. The simulation results predict that there is a low possibility of the multipactor under the TW power with the copper after baking. Such a prediction is consistent with the high-power test result, i.e., a multipactor was not realized under a TW power of 0–143 kW, as introduced in Sect. 3.

Because the windows were tested for both TW and SW powers, the multipactor simulation under SW power was compared with that under TW power. In Fig. 10b, the simulation results show that the beryllia window had a lower number of emitted secondary electrons as compared with the alumina window under both SW and TW powers. In particular, under an SW power of 100 kW, the beryllia window indicated a lower multipactor possibility. Based on the SW test, we discovered a similar level of multipactor-like outgassing in the alumina and beryllia windows. During the SW test, both alumina and beryllia disks were tested at the antinode and $\pm \lambda_g/16$ away from the antinode. In the SW test of the alumina window with 5% RF duty, we observed severe outgassing once the ceramic disk was $\pm \lambda_g/16$ away

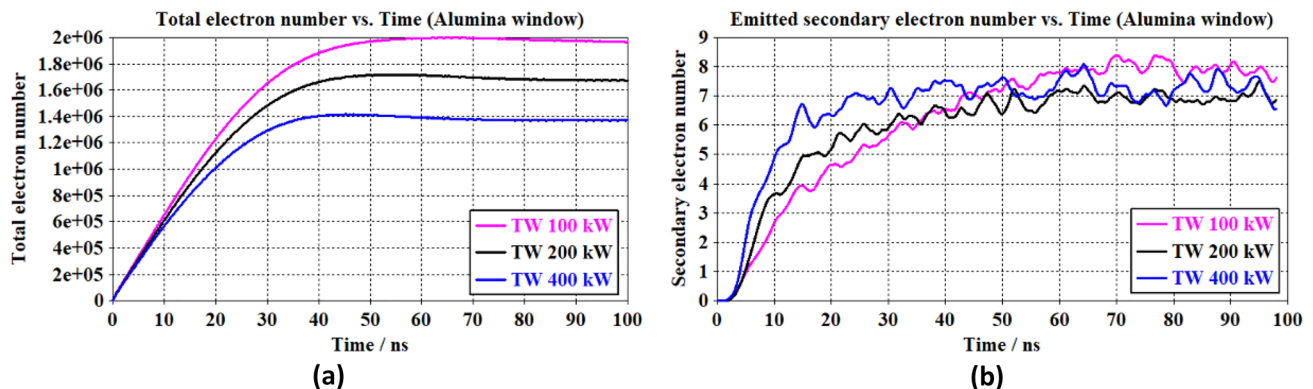
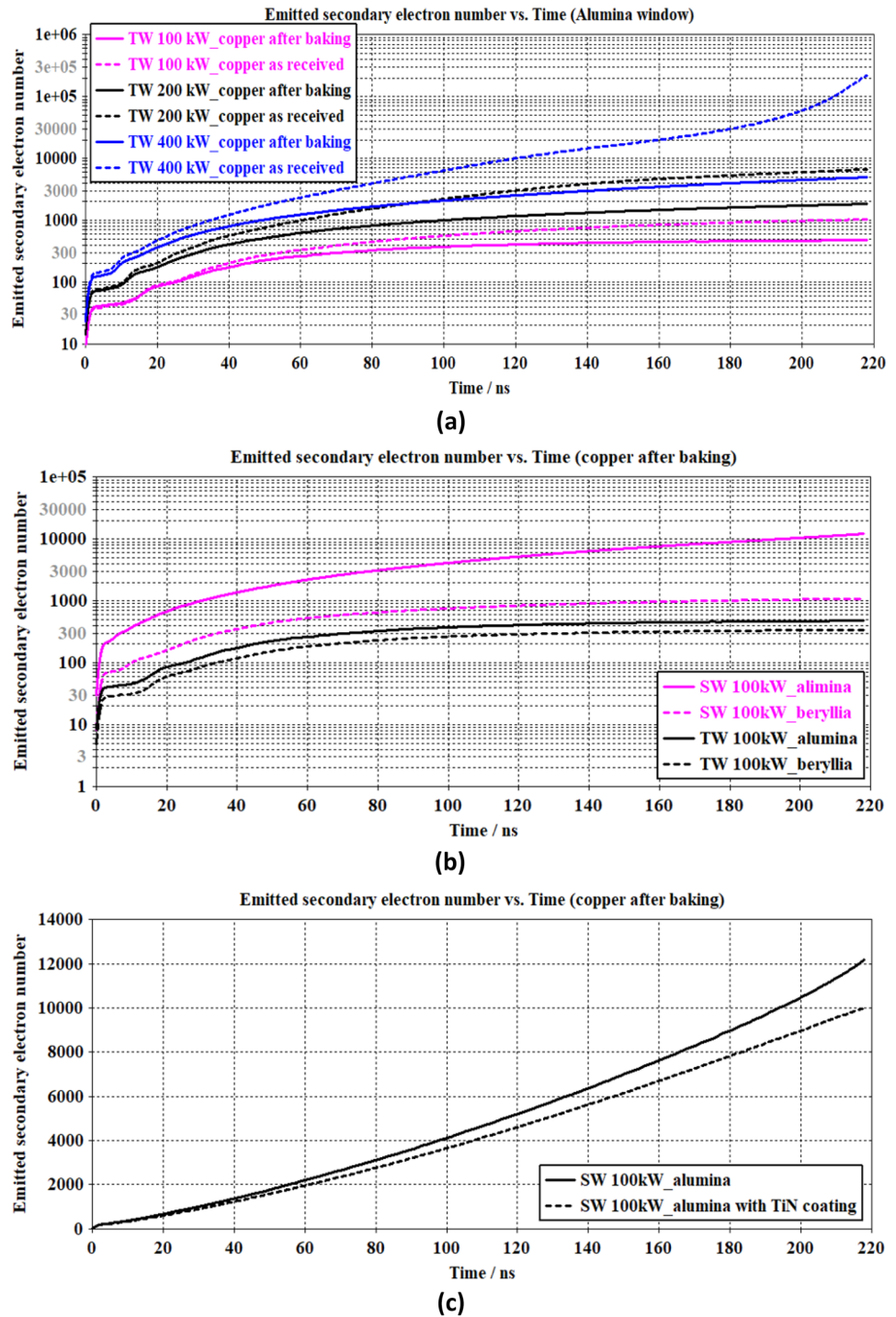


Fig. 9 (Color online) Total and emitted secondary electron numbers vs. time under TW power of 100, 200, and 400 kW from PIC simulation. **a** Total electron number in vacuum of alumina window; **b** emitted secondary electron number from alumina disk

Fig. 10 (Color online) **a** Emitted secondary electron number with as-received copper and after baking under TW power; **b** emitted secondary electron number under SW and TW powers for alumina and beryllia windows; **c** emitted secondary electron number under SW power for alumina and TiN-coated alumina windows



from the antinode. Outgassing was continuous and repetitive, with no indications of a decreasing trend. We suspected that some multipactors were realized even when no glow was captured by the camera. This might be because the RF duty was extremely short or the cameras were not qualified to capture a faint glow. By contrast, the beryllia window did not show any multipactor-like outgassing once the RF shorts shifted by a distance of $\pm\lambda_g/16$. Some multipactor-like

events occurred in the beryllia window in the power range of 30–70 kW once the ceramic was at the antinode; however, the power level increased over this range and outgassing disappeared. In general, the possibility and severity of multipactor formation in the alumina window were higher than those in the beryllia window during the SW test.

In Fig. 10b, the number of emitted secondary electrons under an SW power of 100 kW increased faster than that

under a TW power of 100 kW for both the alumina and beryllia windows. This prediction was verified in the high-power test because we encountered multipactor-like outgassing during the SW test, as compared with the situation in which no indication of a multipactor was reflected in the TW test.

TiN coating on the surface of ceramics is a well-established technique for reducing the SEY [30, 31]. In the simulation, alumina with a 5 nm TiN coating [29] suppressed the possibility of multiple factors, particularly under SW power. As shown in Fig. 10c, the growth of the emitted secondary electrons decelerated when a TiN-coated alumina disk was used under an SW power of 100 kW. Therefore, in this study, the vacuum sides of alumina and beryllia disks were coated with TiN to a thickness of 2–5 nm.

The resonant or ghost mode [23] near the ceramic disk may induce a multipactor [23]. Using the Eigenmode Solver of the CST STUDIO SUITE [12], the local resonant modes were observed at 714 and 720 MHz for the alumina and beryllia windows, respectively. The window is required with a narrow operating bandwidth of 650 ± 0.5 MHz, based on the designed parameters of the CEPC MBK listed in Table 1. Because only one resonant mode was observed below 1 GHz in the vicinity of the ceramic disk and the frequency of the resonant mode was more than 60 MHz away from the operating bandwidth, the resonant mode was not considered problematic.

Because the beryllia window showed a lower possibility of being a multipactor in both the simulation and high-power tests, it should be selected as the output window of the MBK.

5 Conclusion

The 650 MHz thin-pillbox windows were designed for a CEPC MBK. The measured VSWRs for both the alumina and beryllia prototype windows were less than 1.1, based on tolerance analysis and the tuning method. A high-power test validated the proposed window design. By performing a benchmark thermal analysis study, the total heat factor, including the loss tangent of the dielectric disks and the Ohmic loss of the coated antimultipactor layer, was acquired. Predictions from the multipactor simulations were confirmed via a high-power test.

Author contributions All authors contributed to the study conception and design. Material preparation, data collection and analysis were performed by Sheng-Chang Wang. The first draft of the manuscript was written by Sheng-Chang Wang and all authors commented on previous versions of the manuscript. All authors read and approved the final manuscript.

Data Availability The data that support the findings of this study are openly available in Science Data Bank at <https://www.doi.org/10.57760/sciencedb.j00186.00167> and <https://cstr.cn/31253.11.sciencedb.j00186.00167>.

Declarations

Conflict of interest The authors declare that they have no competing interests.

References

- CEPC Study Group, CEPC Conceptual Design Report: Volume 1—Accelerator. (2018). <https://doi.org/10.48550/arXiv.1809.00285>
- S. Wang, S. Fukuda, Z. Lu et al., Design study and modeling of multi-beam Klystron for Circular Electron Positron Collider. *Nucl. Instrum. Meth. A* **1026**, 166208 (2022). <https://doi.org/10.1016/j.nima.2021.166208>
- Z. Zhou, Y. Chen, Y. Chi et al., Progress on CEPC 650 MHz klystron. *Int. J. Mod. Phys. A* **36**, 22 (2021). <https://doi.org/10.1142/S0217751X21420112>
- Y. Ding, Technical status and latest progress of high power klystrons. *Vacuum Electronics* **1**, 1–25 (2020). <https://doi.org/10.16540/j.cnki.cn11-2485/tn.2020.01.01>. (in Chinese)
- M. Pisharody, P. Barnes, E. Chojnacki et al., in *Proceedings of 1995 Particle Accelerator Conference*, Dallas, Texas, 1–5 May 1995.
- R. A. Rimmer, G. Koehler, T. Saleh et al., in *Proceedings of the 2001 Particle Accelerator Conference*, Chicago, Illinois, 18–22 June 2001.
- Z. Gao, L. Lu, C. Xing et al., Design of a 200-MHz continuous-wave radio frequency quadrupole accelerator for boron neutron capture therapy. *Nucl. Sci. Tech.* **32**, 23 (2021). <https://doi.org/10.1007/s41365-021-00859-1>
- G. Liu, Y. Wang, W. Wang et al., Design and measurement of a broadband beryllium oxide window with high power handling capability. *IEEE. Trans. Electron. Dev.* **68**, 9 (2021). <https://doi.org/10.1109/TED.2021.3098252>
- <https://global.kyocera.com>
- <http://www.hongxing799.com>
- R. A. Rimmer, G. Koehler, T. Saleh, et al., 700 MHz window R & D at LBNL, LBNL-47939.
- CST STUDIO SUITE™, www.cst.com
- Z. Ma, J. Chen, Design optimization of 3.9 GHz fundamental power coupler for the SHINE project. *Nucl. Sci. Tech.* **32**, 132 (2021). <https://doi.org/10.1007/s41365-021-00959-y>
- C. Qin, Z. Zhu, Y. Yang et al., Design of 325 MHz high power RF window. *Atomic Energy Sci. Technol.* **54**, 5 (2020). <https://doi.org/10.7538/yzk.2019.youxian.0582>. (in Chinese)
- L. Sun, C. Zhang, A. Shi, et al., in *Proceedings of IPAC2014*, Dresden, 15–20 June 2014.
- F. Zhu, Z. Zhang, J. Luo et al., Investigation of the failure mechanism for an S-Band pillbox output window applied in high-average-power klystrons. *IEEE. Trans. Electron. Dev.* **57**, 4 (2010). <https://doi.org/10.1109/TED.2010.2041874>
- E. Chojnacki, T. Hays, J. Kirchgessner, et al., in *Proceedings of the 1997 Particle Accelerator Conference*, Vancouver, B.C., 12–16 May 1997.
- Z. Ma, S. Zhao, X. Liu et al., High RF power tests of the first 13 GHz fundamental power coupler prototypes for the SHINE project. *Nucl. Sci. Tech.* **33**, 10 (2022). <https://doi.org/10.1007/s41365-022-00984-5>

19. W. Pan, T. Huang, Q. Ma et al., Development of a 500 MHz high power RF test stand. *Chin. Phys. C.* **36**, 4 (2012). <https://doi.org/10.1088/1674-1137/36/4/011>
20. Z. Wang, M. Wang, T. Lei et al., Design of NNBI RF power source output power control system. *Nuclear Techniques* **46**, 010402 (2023). <https://doi.org/10.11889/j.0253-3219.2023.hjs.46.010402>. (in Chinese)
21. F. Yan, H. Geng, C. Meng et al., Commissioning experiences with the Spoke-based CW superconducting proton linac. *Nucl. Sci. Tech.* **32**, 105 (2021). <https://doi.org/10.1007/s41365-021-00950-7>
22. S. Michizono, Secondary electron emission from alumina RF windows. *IEEE Trans. Dielect. Electr. Insul.* **14**, 3 (2007). <https://doi.org/10.1109/TDEI.2007.369517>
23. F. Lin, Y. Ding, B. Shen et al., Research on cylindrical box type windows used to transmit high power CW. *J. Electron. (China)* **21**, 392 (2004). <https://doi.org/10.1007/BF02687940>
24. Z. Ma, W. Chen, Z. Wang et al., Single bunch selection for 162.5 MHz radio-frequency quadrupole accelerator. *Nuclear Techniques* **44**, 050202 (2021). <https://doi.org/10.11889/j.0253-3219.2021.hjs.44.050202>. (in Chinese)
25. G. Liu, Y. Song, G. Chen et al., Design and analysis of RF window for a superconducting cyclotron. *IEEE. Trans. Nucl. Sci.* **65**, 9 (2018). <https://doi.org/10.1109/tns.2018.2861422>
26. G. Burt, R.G Carter, A.C. Dexter et al., in *Proceedings of SRF2009 Conference*, Berlin, 20–25 September 2009.
27. S. Tao, H. Chan, H. Graaf, Secondary electron emission materials for transmission dynodes in novel photomultipliers: a review. *Materials Basel* **9**, 1017 (2017). <https://doi.org/10.3390/ma9121017>
28. V. Baglin, J. Bojko1, O. Gröbner et al., in *Proceedings of EPAC 2000 Conference*, Vienna, 26–30 June 2000.
29. Z. Lu, S. Fukuda, Z. Zhou et al., Design and development of radio frequency output window for circular electron–positron collider klystron. *Chin. Phys. B* **27**, 11 (2018). <https://doi.org/10.1088/1674-1056/27/11/118402>
30. Y. Ding, *Design, Manufacture and Application of High Power Klystron*, 1st edn. (National Defense Industry Press, Arlington, 2010), pp.269–271
31. Z. Peng, G. Chen, Y. Zhao et al., Investigation of TiN film on an RF ceramic window by atomic layer deposition. *J. Vac. Sci. Technol. A* **38**, 052401 (2020). <https://doi.org/10.1116/6.0000159>

Springer Nature or its licensor (e.g. a society or other partner) holds exclusive rights to this article under a publishing agreement with the author(s) or other rightsholder(s); author self-archiving of the accepted manuscript version of this article is solely governed by the terms of such publishing agreement and applicable law.